A Dynamic Mesh-Based Approach to Model Melting and Shape of an ESR Electrode

E. KARIMI-SIBAKI, A. KHARICHA, J. BOHACEK, M. WU, and A. LUDWIG

This paper presents a numerical method to investigate the shape of tip and melt rate of an electrode during electroslag remelting process. The interactions between flow, temperature, and electromagnetic fields are taken into account. A dynamic mesh-based approach is employed to model the dynamic formation of the shape of electrode tip. The effect of slag properties such as thermal and electrical conductivities on the melt rate and electrode immersion depth is discussed. The thermal conductivity of slag has a dominant influence on the heat transfer in the system, hence on melt rate of electrode. The melt rate decreases with increasing thermal conductivity of slag. The electrical conductivity of slag governs the electric current path that in turn influences flow and temperature fields. The melting of electrode is a quite unstable process due to the complex interaction between the melt rate, immersion depth, and shape of electrode tip. Therefore, a numerical adaptation of electrode position in the slag has been implemented in order to achieve steady state melting. In fact, the melt rate, immersion depth, and shape of electrode tip are interdependent parameters of process. The generated power in the system is found to be dependent on both immersion depth and shape of electrode tip. In other words, the same amount of power was generated for the systems where the shapes of tip and immersion depth were different. Furthermore, it was observed that the shape of electrode tip is very similar for the systems running with the same ratio of power generation to melt rate. Comparison between simulations and experimental results was made to verify the numerical model.

DOI: 10.1007/s11663-015-0384-0

I. INTRODUCTION

THE electroslag remelting (ESR) process is used for manufacture of premium-grade steel and super alloys such as Ni-based or titanium alloys. The Joule heating released within the molten slag layer is used to melt a consumable electrode. The departed melt droplets from the tip of electrode pass through the slag and reach the liquid melt pool. The melt pool solidifies finally in a water-cooled mold to build the high-grade, with minimum defect and segregation ingot.[1] Generally, the quality of the ingot is characterized by the surface and internal quality, which depends highly on the shape of melt pool, *i.e.*, the depth and thickness of mushy zone. The desired outcome of the ESR process is a shallow melt pool that promotes unidirectional (upwards) solidification of the ingot and subsequent formation of segregation-minimal alloy.[2] In addition, ingots with good surface quality can be directly forged after the ESR process. The expensive process of surface machining is not required for ESR ingots with smooth surfaces.[3]

The remelting parameters of the ESR process such as melt rate and immersion depth can significantly influence the quality of the final ingot. The influence of melt rate of the electrode on the melt pool depth was investigated by Holzgruber.[4] It was found that the melt pool becomes deeper with the increase of melt rate. In addition, Mitchell[5] studied the effect of melt rate on the pool profile and the thickness of mushy zone for an ESR ingot. The depth of melt pool and thickness of the mushy zone were found to increase when the process was run with higher melt rate. On the other hand, a relatively smooth ingot surface can be obtained with higher melting rate as reported by Suarez *et al.*[6] Furthermore, it is believed that maintaining a constant shallow immersion depth of the electrode leads to producing superior quality ingots.[7] As stated by Kharicha *et al.*,[8] the surface quality of ingot is significantly influenced by distribution of mold current in the process that in turn depends on the electrode immersion depth.

As a consequence, the improper control of immersion depth can severely influence the compositional homogeneity and grain structure of the solidified ingot. Currently, there is no system or method for the direct measurement of the melt rate and immersion depth of electrode. Practically, the immersion depth is controlled

E. KARIMI-SIBAKI, Ph.D. Student, is with the Christian Doppler Laboratory for Advanced Process Simulation of Solidification and Melting, University of Leoben, Leoben, Austria. A. KHARICHA, Senior Scientist, and M. WU, Associate Professor, are with the Christian Doppler Laboratory for Advanced Process Simulation of Solidification and Melting, University of Leoben, and also with the Chair of Simulation and Modeling of Metallurgical Processes University of Leoben. Contact e-mail: abdellah.kharicha@unileoben.ac.at J. BOHACEK, Postdoctoral Researcher, and A. LUDWIG, Professor, are with the Chair of Simulation and Modeling of Metallurgical Processes University of Leoben.
Manuscript submitted December 3, 2014.

Published online: 11 June 2015

based on the variation of impedance or voltage (voltage swing) during the process.[9–12] In this way, the increase of impedance swing is quantitatively related to the immersion depth. However, fluctuations of immersion depth are observed over the standard swing controller in many instances during the process. Therefore, the measurement precision of the actual immersion depth is questionable.

During the ESR process, a massive amount of heat generated in the slag is lost through radiation and mold cooling. Only a small portion of power is supplied to melt the electrode. Over the last decades, attempts have been made to investigate the temperature profile, immersion depth, melt rate, and the shape of electrode. The effects of input power and electrode polarity on the melt rate and shape of the electrode tip were experimentally investigated by Maulvault.[13] It is reported that increasing the input power leads to higher melting speed and subsequently to a flattening of electrode tip. Mitchell *et al.*[14] proposed a two-dimensional model to study the heat balance across the electrode. The immersion depth is taken into account to compute the steady state temperature profile of the electrode. In addition, the electrode temperature gradient was experimentally measured for a laboratory scale ESR process. The model agreed successfully with the experimental results. A one-dimensional analytical model was developed by Mendrykowski *et al.*[15] to study the heat transfer above and below the slag level. Their computed results suggest that thermal radiation is negligible in comparison to the heat conduction along the electrode. A good agreement is observed between the calculated and measured temperature profile within the electrode. Kishida *et al.*[16] reported the relationship between the immersion depth, shape of the electrode tip, and voltage drop for a small scale ESR process. They found that with the increase of voltage, the immersion depth decreases and the shape of the electrode tip becomes flatter. Tacke and Schwerdtfeger[17] used a two-dimensional numerical model to compute the temperature, pool profile, and immersion depth for a laboratory scale ESR electrode. An approximation formula for the immersion depth was proposed and validated against experiments.

Jardy *et al.*[18] modeled the ESR process to evaluate thermal fluxes through boundaries. Their model predicted the highest melt rate for the case where the buoyance force is stronger than electromagnetic force. Yanke *et al.*[19] predicted melting behavior of an industrial ESR process using an effective heat transfer coefficient between electrode and slag. Their results were fairly similar to measured data.

Recently, Kharicha *et al.*[20] directly simulated the melting of electrode using the multiphase volume of fluid (VOF) method considering complex interactions between flow, temperature, and magnetic fields. It is found that the coupling between the Joule heat release and melting rate is very unstable. Furthermore, it is shown that the stability in simulation can be achieved only by including a numerical adaptation on immersion depth and feeding velocity of electrode. Within the framework of the multiphase model, details of process conditions such as temperature, velocity, and magnetic force can be captured. However, the method used in this investigation is computationally expensive.

It is generally recognized that the electric current is conducted by ions in the slag region.[21] The melt rate was reported to be dependent on electrode polarity. During DC ESR process, smaller current is required for electrode positive in comparison to electrode negative to achieve the same melt rate, even though the voltage is kept unchanged.[22] The highest specific melt rate is obtained using positive polarity for electrodes containing high oxide concentrations (>10 wt pct) due to the increase of electrochemical polarization overpotential at electrode tip–slag interface.[21] There are other phenomena that can influence the amount of supplied heat to electrode tip and consequently melt rate. For instance, a thin liquid film is formed related to formation and departure of droplets at electrode tip during remelting. Furthermore, droplets drip through the slag and they intensify turbulence under the electrode tip. As a consequence of strong turbulence, reaction rate and heat transfer between the remelting electrode and slag are enhanced.[23,24]

The present model is an extension of electromagnetic model developed by Kharicha for ESR process.[12,20] Here, a dynamic mesh-based approach is used to predict the shape and melt rate of the electrode. The method is robust and computationally efficient. Effects of electrochemical polarization overpotential, formation of liquid film near the electrode tip, and dripping of droplets in slag bath are not included in the current model. Solidification of liquid metal in melt pool is ignored. Simulations considering different electric current paths (with and without mold current) are performed and compared. Furthermore, the influence of electric conductivity and molecular thermal conductivity of slag on the melt rate and shape of electrode tip are investigated. Experimental results of Tacke and Schwerdtfeger[17] are used to evaluate the current model.

II. MODELING

The commercial CFD software, FLUENT-ANSYS v.14.5, is used with a finite volume approach to simulate the fluid flow, heat transfer, and electromagnetic fields. The software includes a dynamic mesh technique for the simulation of displacements of boundaries. The required modeling equations for boundaries (stationary and moving) and fields (*e.g.,* electromagnetic field) are implemented using user-defined functions (UDF). Transient calculation is made to predict the evolution of shape of electrode tip. The induced magnetic field is dominantly azimuthal and the process conditions are assumed to be mainly axisymmetric;[25] thus, a 2D axisymmetric computational domain is considered. Configuration of the computational domain and boundaries are schematically illustrated in Figure 1(a).

A. *Governing Equations*

The computational domain includes zones of air, electrode, slag, melt pool, and mold. Each zone is

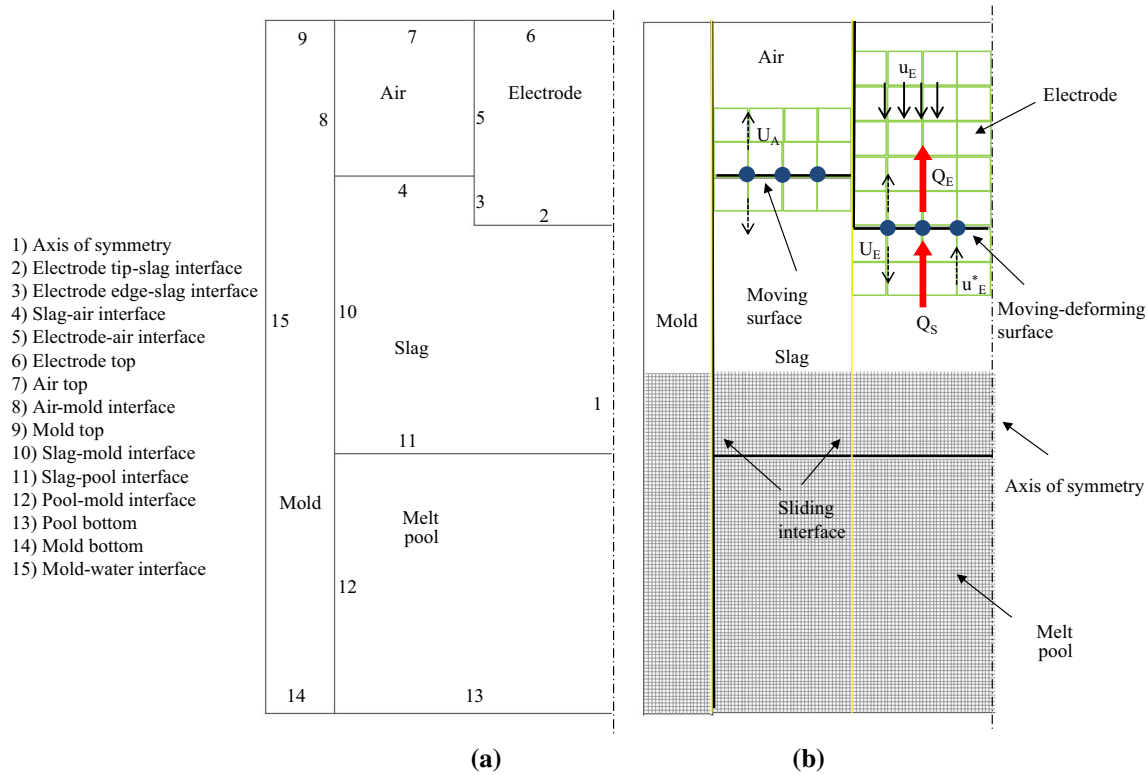

Fig. 1—(*a*) Schematic representation of computational domain and boundaries, (*b*) Conceptual illustration of heat balances across the electrode tip and velocity of grid nodes at electrode tip–slag and slag–air interfaces. The mesh resolution is very high with equisized cells in the whole domain as shown partly in mold, slag, and melt pool. Note that the mesh resolution is shown exaggeratedly coarse near the electrode tip–slag interface (moving–deforming surface) and slag–air interface (moving surface) for illustrative purpose.

Table I. Thermal and Electrical Boundary Conditions

Air top: $T = 300$ K (27 °C), $\frac{\partial \phi}{\partial z} = 0$, $\frac{\partial A_z}{\partial z} = \frac{\partial A_r}{\partial z} = 0$
Electrode top: $T = 900$ K (627 °C), $-\sigma \frac{\partial \phi}{\partial z} = \frac{I_0}{\pi R_e^2}$, $\frac{\partial A_z}{\partial z} = \frac{\partial A_r}{\partial z} = 0$
Slag–air interface: $\varepsilon_r = 0.8$, $H = 50$ W m^{-2} K^{-1}
Slag–mold interface (slag side): $T = 1725$ K (1452 °C)
Slag–mold interface (mold side): $H = 500$ W m^{-2} K^{-1}
Pool–mold interface (pool side): $T = 1725$ K (1452 °C)
Pool–mold interface (mold side): $H = 500$ W m^{-2} K^{-1}
Pool bottom: $T = 1725$ K (1452 °C), $\phi = 0$, $\frac{\partial A_z}{\partial z} = \frac{\partial A_r}{\partial z} = 0$
Mold–water interface (with mold current):
$H = 7000$ W m^{-2} K^{-1}, $\frac{\partial \phi}{\partial z} = 0$, $\frac{\partial A_z}{\partial z} = \frac{I_0}{2\pi R_m}$, $A_r = 0$,
Mold top: $\frac{\partial \phi}{\partial z} = 0$, $\frac{\partial A_z}{\partial z} = \frac{\partial A_r}{\partial z} = 0$
Mold bottom: $\phi = 0$, $\frac{\partial A_z}{\partial z} = \frac{\partial A_r}{\partial z} = 0$

treated separately. However, the transport phenomena at interfaces such as momentum or heat transfer are taken into account. The interface between zones can be rigid, deforming, moving, or stationary. The governing equations and the boundary conditions are introduced in the following sections. A summary of thermal and electrical boundary conditions is given in Table I.

1. *Electromagnetic field*

The A–ϕ formulation is used to calculate the electromagnetic field,[20] where ϕ denotes the electric scalar potential and $\vec{A}$ is the magnetic vector potential. The method is computationally more expensive in comparison to the common approach based on electromagnetic induction equation (B_θ), but the A–ϕ formulation is very robust and accurate for solving electromagnetic field in the presence of moving boundaries. In addition, it can effectively model the current path including mold current and eddy current. The electric scalar potential is obtained by solving the conservation equation of electric current:

$$\nabla \cdot \vec{j} = 0. \qquad [1]$$

The treatment of current density ($\vec{j}$) includes two parts:

$$\vec{j} = -\sigma \nabla \varphi - \sigma \frac{\partial \vec{A}}{\partial t}. \qquad [2]$$

First, the imposed current is computed as a function of electric conductivity of material (σ) and electric scalar potential. The second term includes the effect of eddy currents generated in the process. Note that, the unsteady term in the right-hand side of Eq. [2] can be omitted when the process approaches steady state and a direct current (DC) is applied.

The magnetic field ($\vec{B}$) is calculated by solving the equation of magnetic vector potential that is expressed as

$$\nabla \times \left(\frac{1}{\mu_0} \nabla \times \vec{A} \right) = \vec{j}, \qquad [3]$$

$$\nabla \times \vec{A} = \vec{B}. \quad [4]$$

Note that, to obtain a unique solution for Eq. [3], the Coulomb gauge ($\nabla \cdot \vec{A} = 0$) is used.[26] Additionally, the displacement currents are ignored and the magnetic permeability (μ_0) is assumed to be constant ($4\pi \times 10^{-7}$ J m^{-1} A^{-2}). Finally, the Joule heating (Q) and Lorentz force ($\vec{F}_L$) are computed and added as source terms to the energy and momentum conservation equations, respectively.

$$Q = \frac{\left|\vec{j}\right|^2}{\sigma}, \quad [5]$$

$$\vec{F}_L = \vec{j} \times \vec{B}. \quad [6]$$

The required boundary conditions for electric scalar potential and magnetic vector potential (axial and radial components) are obtained from Eqs. [2] and [4]. A magnetic induction flux of zero is used at the bottom boundaries (mold and pool) and top boundaries (air, mold, and electrode). Additionally, a value of zero is applied for electric scalar potential at the bottom boundaries. However, an electric potential flux of zero is used at top boundaries (air and mold) except electrode top where the flux of electric potential is prescribed. The electric scalar potential is treated similar to the mold top boundary at mold–water interface where axial component of magnetic induction flux is prescribed. The latter takes the value zero for the radial component of magnetic vector potential. Furthermore, continuity of electric and magnetic potentials is applied at the following interfaces: electrode tip–slag, electrode edge–slag, electrode–air, air–mold, slag–air, slag–mold, slag–pool, and pool–mold. It should be stated that the electric current is allowed to cross the slag skin entering into the mold (mold current). In the case of insulating mold (without mold current), the slag–mold, air–mold, and pool–mold interfaces take similar boundary conditions as mold–water interface.

2. *Temperature field*

The temperature field is obtained by solving an enthalpy (h) conservation equation:

$$\frac{\partial}{\partial t}(\rho h) + \nabla \cdot (\rho \vec{u} h) = \nabla \cdot (\lambda \nabla T) + Q - S_{LH}, \quad [7]$$

where ρ is the density, $\vec{u}$ the velocity, and λ the effective thermal conductivity including the effect of turbulence. S_{LH} denotes the energy sink required to melt the electrode in the vicinity of electrode tip, and it is further described in Section II–C.

A combined radiation–convection condition is applied to model the heat transfer between electrode and air, and between slag and air, where a value of 0.8 is used for emissivity. At the top boundaries, the temperature is fixed: 300 K (27 °C) at mold and air top, and 900 K (627 °C) at electrode top. The latter is calculated based on the electrode feeding velocity and distance from the electrode tip.[20] In addition, temperature is fixed at the slag liquidus temperature that is 1725 K (1452 °C) at the following interfaces: slag–mold (slag side) and pool–mold (melt pool side). Assuming a constant thickness of solidified slag skin layer (1 mm), the heat conduction through the slag skin at slag–mold (mold side) and pool–mold (mold side) interfaces is taken into account. The cooling condition at mold–water interface is modeled using a constant convective heat transfer coefficient (7000 W m^{-2} K^{-1}). The restricted maximum allowable temperature at electrode tip–slag and electrode edge–slag interfaces is the melting temperature of the alloy. In addition, the two sides of the wall at slag–pool interface are thermally coupled.

3. *Turbulent flow field*

The continuity and momentum equations are solved:

$$\frac{\partial \rho}{\partial t} + \nabla \cdot (\rho \vec{u}) = 0, \quad [8]$$

$$\frac{\partial}{\partial t}(\rho \vec{u}) + \nabla \cdot (\rho \vec{u}\vec{u}) = -\nabla p + \nabla \cdot \left(\mu\left(\nabla \vec{u} + \nabla \vec{u}^T\right)\right) + \rho_0 \vec{g} \beta (T - T_0) + \vec{F}_L, \quad [9]$$

where p is the pressure, μ the dynamic viscosity, $\vec{g}$ the gravity, β the thermal expansion coefficient, and ρ_0 and T_0 are reference density and reference temperature, respectively. Boussinesq approximation is considered for the thermal convection in the slag region.

Non-slip boundary condition is applied at electrode edge–slag, electrode tip–slag, and slag–pool interfaces. Additionally, a free-slip condition is applied for the interfaces of slag–air, slag–mold, and pool–mold. No flow calculation is made in the air zone. Treatment of velocity inside the electrode will be discussed in Section II–D.

The turbulence is considered using the shear stress transport model (SST). The model is known to effectively blend the precision and robustness of k–ω model in the near-wall region with the bulk liquid k–ε modeling in far field. One of the essential features of SST model is an accurate and effective near-wall treatment. The model is insensitive to the grid spacing of the near-wall cells.[27] In fact, the model automatically shifts from low-Re formulation to wall functions based on the near-wall grid resolution. A comprehensive description of the model was given by Menter.[28,29]

B. *Dynamic Mesh*

Displacement of domain boundaries can be modeled using dynamic and deformable meshes in which the mesh nodes are adjusted to new locations. In order to apply this technique, all governing conservation equations must be modified according to the velocity of the grid boundaries ($\vec{u}_g$).[30] The integral form of the general conservation equation for an arbitrary variable (ξ) with respect to the dynamic meshes is expressed as

$$\frac{\partial}{\partial t}\int_V \rho\xi \mathrm{d}V + \int_\Omega \rho\xi(\vec{u}-\vec{u}_g)\cdot \mathrm{d}\vec{S} = \int_\Omega \Gamma \nabla\xi \cdot \mathrm{d}\vec{S} + \int_V S_\xi \mathrm{d}V, \quad [10]$$

where Ω represents the boundary of the control volume (V), $\vec{S}$ is the area vector, Γ denotes the diffusion coefficient, and S_ξ is the source term.

The unsteady term in Eq. [10] must take into account the variation of cell sizes during the simulation of moving boundaries.[31] It can also be computed using the grid velocity:

$$\frac{\partial V}{\partial t} = \int_\Omega \vec{u}_g \cdot \mathrm{d}\vec{S} = \sum_j^{n_f} \vec{u}_{g,j} \cdot \vec{S}_j, \quad [11]$$

where n_f is the number of faces on the control volume, $\vec{u}_{g,j}$the velocity, and $\vec{S}_j$ is the area vector of j face.

A number of dynamic mesh schemes are available to handle the boundary motion that categorize into layering, re-meshing, and smoothing techniques. In the present study, layering and smoothing techniques are employed to simulate the motion of the boundaries. Essentially, layering technique involves creation and destruction of cell rows in the vicinity of a moving boundary. Layers of cells are added or removed based on a prescribed cell height (h_{ideal}) that is in the same order of magnitude as the cell size. The layer of cell near to the moving boundary is allowed to expand or compress if the following condition is fulfilled: $(1 + \alpha_s)h_{\mathrm{ideal}} < h_{\mathrm{min}}$ for expansion and $h_{\mathrm{min}} < \alpha_c h_{\mathrm{ideal}}$ for compression. Here, h_{min} is the minimum cell height of the neighboring layer, and α_s and α_c are the user-defined split and collapse factors, respectively. The method can be applied only for structured grid when the motion is purely linear like the motion of a piston in a cylinder.

On the other hand, the smoothing technique is not restricted to structured mesh. The nodes can be repositioned but the connectivity remains unchanged. Additionally, they are considered as a network of interconnected springs in which positions of interior nodes are updated based on displacements of boundary nodes. The diffusion-based smoothing method to model the mesh motion is governed by the following equation:

$$\nabla \cdot \left(\frac{1}{d^\alpha}\nabla \vec{u}_g\right) = 0, \quad [12]$$

where d stands for a normalized boundary distance and α is a positive arbitrary input parameter. Note that, quality of the mesh can be better preserved by increasing the diffusivity coefficient ($1/d^\alpha$). Thus, a value of zero is recommended for α to reduce the mesh motion away from the moving boundary.[30]

The configuration of the dynamic mesh boundaries is illustrated in Figure 1(b). In our computational domain, the mesh has two dynamic boundaries: slag–air (moving) and electrode tip–slag (moving–deforming). The moving boundaries are interior faces; thus, sliding interfaces are required to allow the relative motion between adjacent grids.[30] Geometrical data of dynamic mesh parameters are listed in Table II.

Table II. Geometrical Data of Mesh and Dynamic Mesh Parameters

Mesh	
Domain size (mm^2)	100 × 200
Number of computational cell	20,000
cell size (mm)	1
Ideal cell height (mm)	1
Split factor (α_s)	0.4
Collapse factor (α_c)	0.2
Diffusion parameter (α)	0

C. *Melting of Electrode Tip*

Both the temperature field of electrode and velocity of melting electrode tip are unknown. Generally, an alloy solidifies and develops a dendritic mushy zone. However, no dendrites were observed during melting. Thus, the liquid–solid interface is assumed to remain smooth during melting. Therefore, the melting of the electrode is considered as a Stefan problem where a phase boundary can move with time.[32,33] Here, a dynamic mesh-based approach is proposed to capture the shape of the electrode tip. A set of balance equations are solved to compute the velocity of grid nodes at the electrode tip. As shown in Figure 1(b), the heat balance across the electrode tip determines the velocity of the grid nodes (U_E). The following equations and conditions describe the melting velocity of electrode tip:

$$Q_S - Q_E = \rho_{\mathrm{metal}} \Delta H u_E^*, \quad [13]$$

$$\begin{cases} u_E^* \geq 0 & (Q_S > Q_E) \\ u_E^* < 0 & (Q_S < Q_E) \end{cases}, \quad [14]$$

$$U_E = u_E + u_E^*. \quad [15]$$

According to Eq. [15], the time-dependent grid node velocity of the electrode tip is the sum of melting velocity (u_E^*) and the electrode feeding velocity (u_E). The origin of x-referential is fixed at the bottom of computational domain. Consequently, the sign (positive or negative) of melting velocity depends on the balance of the heat fluxes at the electrode tip, Eq. [14]. According to Eq. [13], the melting velocity is dependent on the heat flux provided to electrode (Q_S), heat flux diffused into the electrode (Q_E), density of metal (ρ_{metal}), and latent heat of fusion (ΔH). Note that the right-hand side of Eq. [13] describes the energy sink term (S_{LH}) provided to melt the electrode. The following equation expresses the volumetric source of latent heat that is absorbed in the vicinity of electrode tip.

$$S_{LH} = \rho_{\mathrm{metal}} u_E^* \Delta H \left(\frac{S_{\mathrm{cell-electrode}}}{V_{\mathrm{cell-electrode}}}\right), \quad [16]$$

where $S_{\text{cell-electrode}}$ is the face area of a cell which belongs to the electrode tip and $V_{\text{cell-electrode}}$ is the cell volume.

D. *Electrode Immersion Depth*

Ideally, the electrode feeding velocity is constant during operation of the ESR process. However, the feeding velocity must be adapted in the simulation due to melting instabilities so that the electrode tip neither reaches the melt pool nor the slag-free surface.[20] The electrode feeding velocity is adapted based on the initial feeding velocity (u_{E}^{0}) and immersion depth (l) as given by Eq. [17].

$$u_{\text{E}} = u_{\text{E}}^{0} \min\left[1, \frac{l_{\max} - l}{l_{\max} - l_{\min}}\right]. \qquad [17]$$

The immersion depth is bounded between $l_{\min}$ and $l_{\max}$, and both are input parameters. As such, the electrode penetration depth is limited to $l_{\max}$. Note that, the uniform velocity field inside the electrode zone is specified that has the magnitude equal to the electrode feeding velocity (u_{E}).

Transient simulation is performed until a steady state is reached when the velocity of the grid nodes (U_{E}) becomes zero. The melt rate ($\dot{m} \geq 0$) of the electrode can be estimated as

$$\dot{m} = -\rho_{\text{metal}} \iint_{S_{\text{electrode}}} \vec{u}_{\text{E}}^{*} \cdot \mathrm{d}\vec{S}, \qquad [18]$$

where $S_{\text{electrode}}$ is the tip area of electrode.

With the increase of electrode immersion depth, the slag level rises since the total mass of slag must be conserved. The latter is modeled by considering a constant velocity for the grid nodes at slag–air interface. The velocity of slag–air interface (U_{A}) is computed as

$$U_{\text{A}} = \frac{m_0 - m}{\rho_{\text{slag}} \Delta t (S_{\text{mold}} - S_{\text{electrode}})}, \qquad [19]$$

where m_0 is the initial mass of slag, m the computed mass, ρ_{slag} density of slag, Δt time step size, and S_{mold} denotes the cross-sectional area of mold. Note that, the grid node velocity (U_{E}) weakly fluctuates around zero once the process reaches the steady state.

E. *Simulation Setup*

The physical properties of the materials are listed in Table III. The shape of electrode tip is mainly governed by the thermal field and flow in the slag region; hence, the electrical and thermal properties of slag play an important role. The slag has the following composition: 40 pct CaF_2, 30 pct CaO, 30 pct Al_2O_3.[17] The electric or thermal conductivities of the slag are temperature dependent,[34] but due to the difficulty of the measurement, a large uncertainty of the properties exists. The electric conductivity of conventional slags in liquid state was reported to vary between 80 and 300 Ω^{-1} m^{-1}.[35] The electric conductivity of the slag in solid state is even unknown. The solidified slag skin layer formed on the mold wall is assumed to be a perfectly electrical insulator in most of simulations found in the literature.[25,36,37] On the other hand, it is observed that considerable amount of current can cross the solid slag skin (mold current) entering into the mold despite low electric conductivity of the layer.[22,38–45] Simulations considering different current paths are performed and details of analyses are given in next section. The rate of heat transfer between molten slag and mold, air, or electrode is governed by thermal conductivity. The latter significantly influences the temperature field in the process. Approximate values for thermal conductivity of CaF_2-based slags at elevated temperatures are reported to be between 0.5 and 5 W m^{-1} K^{-1}.[46] Therefore, parameter studies by varying the thermal conductivity of slag are also made. Table IV describes conditions for parameter studies.

Tacke and Schwerdtfeger conducted a series of experiments to investigate the influence of operation parameters on the shape of electrode tip for a laboratory scale ESR process.[17] Here, we use the identical geometry for the simulations, and compare the simulation results with one of their experiments (Table V).

III. RESULTS

A. *Transient Melting of Electrode*

Here, the capability of model to capture the shape of electrode during remelting is demonstrated. Transient

Table III. Physical Properties of Materials

Slag	
Density (kg m^{-3})	2700
Viscosity (kg m^{-1} s^{-1})	0.0025
Specific heat (J kg^{-1} K^{-1})	1500
Thermal exp. coefficient (K^{-1})	9×10^{-5}
Thermal conductivity, liquid (W m^{-1} K^{-1})	variable (Table IV)
Electric conductivity, liquid (ohm^{-1} m^{-1})	variable (Table IV)
Steel	
Density (kg m^{-3})	7100
Viscosity (kg m^{-1} s^{-1})	0.006
Specific heat, liquid (J kg^{-1} K^{-1})	800
Thermal exp. coefficient (K^{-1})	0.0001
Latent heat of fusion (J kg^{-1})	260,000
Thermal conductivity (W m^{-1} K^{-1})	40
Electric conductivity (ohm^{-1} m^{-1})	880,000
Air	
Density (kg m^{-3})	1.2
Viscosity (kg m^{-1} s^{-1})	1.7×10^{-5}
Specific heat (J kg^{-1} K^{-1})	1000
Thermal conductivity (W m^{-1} K^{-1})	0.02
Electric conductivity (ohm^{-1} m^{-1})	10^{-10}
Copper	
Density (kg m^{-3})	8500
Specific heat (J kg^{-1} K^{-1})	381
Thermal conductivity (W m^{-1} K^{-1})	300
Electric conductivity (ohm^{-1} m^{-1})	4×10^{7}

Table IV. Conditions of Parameter Studies

	Slag Electric Conductivity, Liquid (ohm^{-1} m^{-1})	Slag Thermal Conductivity, Liquid (W m^{-1} K^{-1})	Mold Current
Case I	250	5	no
Case II	250	5	yes
Case III	170	1.5	yes
Case IV	170	5	yes

Table V. Operation conditions and results of a laboratory scale ESR process,[17] and comparison with simulations (steady state)

	Experiment[17]	Case I	Case II	Case III	Case IV
Electric current mode	DC	DC	DC	DC	DC
Electric current (kA)	1.9	1.9	1.9	1.9	1.9
Mold current	unknown	no	yes	yes	yes
Electrode radius (cm)	4	4	4	4	4
Mold radius (cm)	8	8	8	8	8
Slag weight (kg)	4.0	4.1	4.1	4.1	4.1
Slag e-cond. (ohm^{-1} m^{-1})	unknown	250	250	170	170
Slag ther. cond.(W m^{-1} K^{-1})	unknown	5	5	1.5	5
Voltage (V)	29	28	15	23	22
Power generation (kW)	55	55	28	43	40
Initial feeding vel. (cm s^{-1})	unknown	0.0153	0.0153	0.0153	0.0153
Steady feeding vel. (cm s^{-1})	0.0153	0.007	0.0063	0.0116	0.0045
Melt rate (g s^{-1})	5.5	3.1	2.2	4.1	1.7
Immersion depth (cm)	3.8	3.6	3.5	2.9	4.0
Power consumption (kJ g^{-1})	10	18	12.7	10.5	23
L_{min} (cm)	unknown	2.5	2.5	2.5	2.5
L_{max} (cm)	unknown	4.5	4.5	4.5	4.5

behavior of process for one case study (Case I) is discussed in details considering interactions between flow field, temperature field, electromagnetic field, and shape of electrode. The evolution of electrode shape as well as electric potential, temperature, and velocity fields are illustrated in Figure 2. Additionally, the mesh resolution near moving–deforming boundary (electrode tip–slag interface) is shown. The magnitude of voltage drop and subsequently power generation is strongly dependent on immersion depth of electrode (maximum distance between electrode tip and slag–air interface). As a result of higher voltage drop at lower immersion depth, the power generation increases in the system. Consequently, the temperature rises in the slag at low immersion depth as shown in Figure 2(c). Furthermore, the velocity is increased under the shadow of electrode at higher immersion depth as shown in Figures 2(d) through (f). The current density increases at larger immersion depth under the electrode that intensifies the Lorentz force. Thus, the velocity becomes higher in central region of slag where stirring is promoted and the temperature field is relatively uniform.

We have previously found that the coupling between melt rate and power generation due to Joule heating is very unstable.[20] This fact is verified in this study again. As shown in Figure 3(d), the ratio of the power generation to melt rate, called power consumption, changes during the whole remelting process. In addition to that the immersion depth, melt rate, and power generation are also plotted in Figures 3(a) through (c). The results reveal that variation in power is much gentler than the variation of melt rate. In other words, the melt rate can change dramatically although the power generation remains relatively stable before reaching the steady state (>900 seconds). Furthermore, the peak is observed in the power generation when the immersion depth becomes very shallow, Figure 3(a). Essentially, power generation and immersion depth oppose each other as shown in Figures 3 (a) and (b). In other words, the power generation is higher at lower immersion depth and vice versa.

In summary, the model enables us to study the dynamic interactions between velocity field, temperature field, electromagnetic field, and shape of electrode tip during remelting. Additionally, melting parameters such as melt rate, immersion depth, power generation, and power consumption can be directly computed.

B. *Parameter Studies*

Four cases are simulated (Table IV). Following the experiment[17], a DC current is imposed and kept constant. The initial feeding velocity of the electrode (not reported for the experiment) is assumed and kept unchanged for all simulation cases. Note that two extreme cases might occur when an improper feeding velocity is applied. One is that the electrode tip might totally leave out of the slag during operation when a

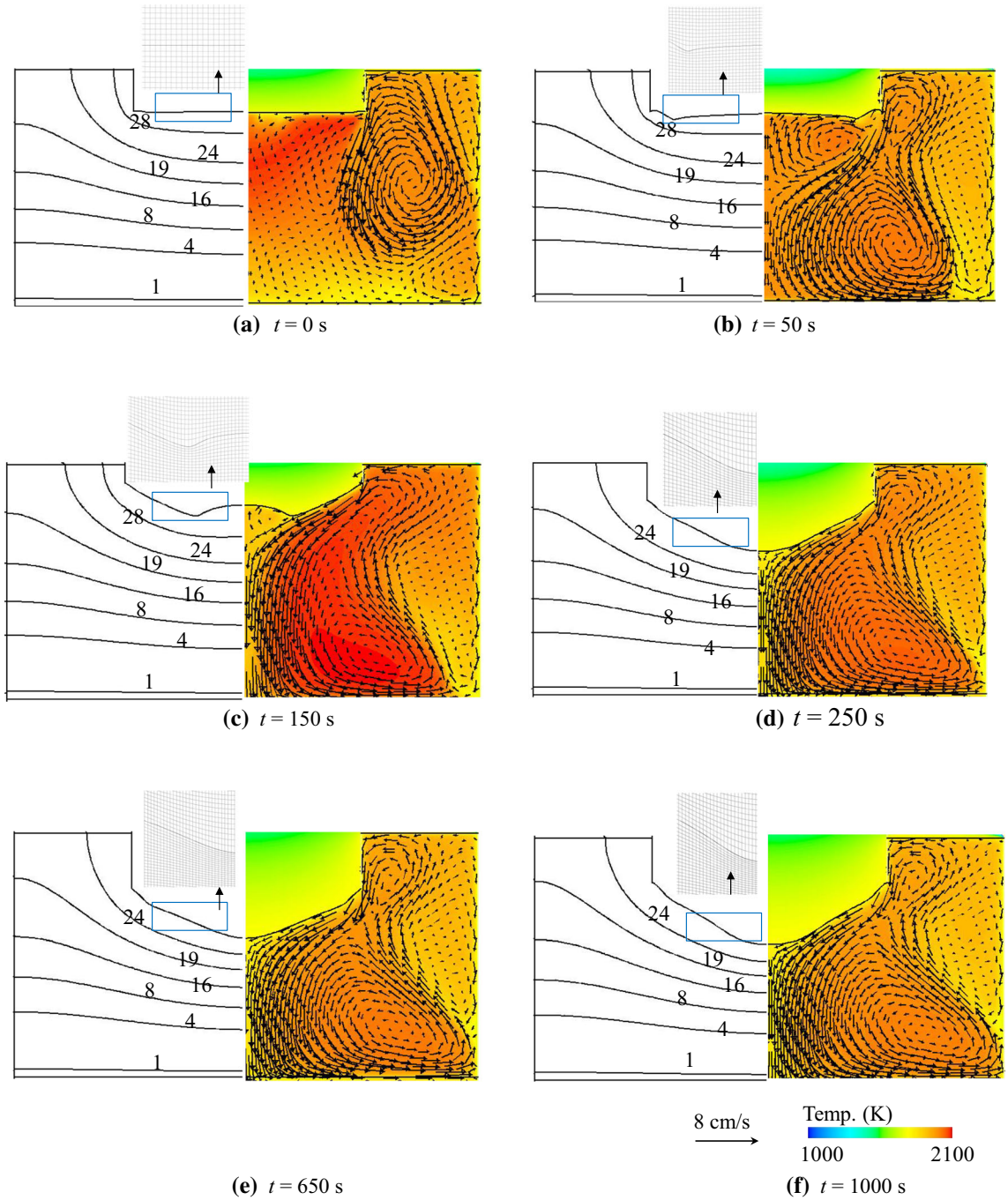

Fig. 2—Modeling result of evolution of shape of electrode tip for Case I: (*a*) $t = 0$, (*b*) $t = 50$ s, (*c*) $t = 150$ s, (*d*) $t = 250$ s, (*e*) $t = 650$ s, (*f*) $t = 1000$ s. On left half: Isolines of voltage and the grid near the moving–deforming boundary (electrode tip–slag interface). On right half: Contour of temperature overlaid with vectors of velocity in the slag region.

very low feeding velocity is applied for a case with large melt rate. The another extreme case is that the electrode tip might touch the slag–pool interface when very high feeding velocity is applied for a case of low melt rate, which leads to an electrical shortcut between the electrode tip and molten metal pool. Therefore, the feeding velocity of the electrode must be adjusted according to Eq. [17] to avoid the aforementioned undesirable extreme cases. In the operation, the initial feeding velocity is unknown, but the feeding velocity at steady state is known. The steady state feeding velocity was extracted from the simulations for the case studies. In addition, the melt rate is calculated using Eq. [18]. The amplitude of voltage and power depends on the current density and shape of the tip that are reported at the steady state. A summary of case studies at the initial and steady states are shown in Figures 4 and 5. In addition, temperature, velocity, voltage, and current density fields including the submerged part of electrode in slag zone are provided.

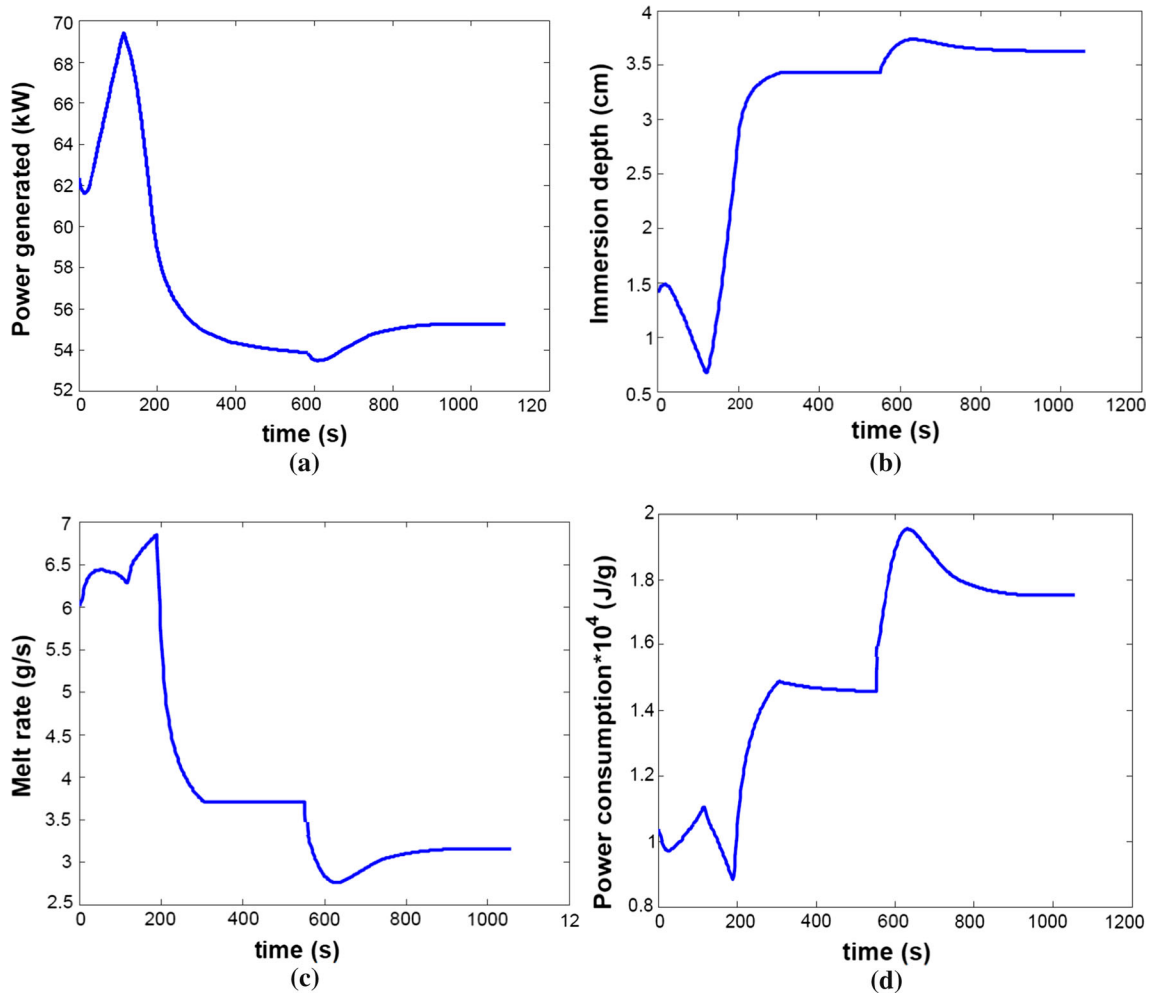

Fig. 3—Analysis of melting parameters for Case I: (*a*) power generation, (*b*) immersion depth, (*c*) melt rate, (*d*) power consumption (ratio of power generation to melt rate).

1. *Case I*

The melting of electrode for this case was previously discussed in details in Section III–A. A high electrical conductivity and high thermal conductivity of the liquid slag are assumed (Table IV). The solidified slag layer near the mold wall is assumed to be an electrical insulator and no current enters into mold. The isolines of voltage in the beginning of simulation and final steady state are compared as shown in Figure 4 (Case I). With the increase of immersion depth, the isolines of voltage are shifted and the voltage of system is reduced. In addition, the maximum amount of current density is initially observed near the edge of electrode. However, the amplitude of current density is increased in the slag zone under the shadow of electrode for the deeply submerged electrode. As a consequence, the Lorentz force becomes stronger that results in promotion of stirring and intensification of velocity under the electrode. The amount of generated power due to Joule heating is significant (Table V) leading to a high temperature in the slag zone. In addition, the electrode tip deforms to a parabolic shape.

2. *Case II*

A high electrical conductivity and high thermal conductivity of the liquid slag are assumed, as same as Case I, but the current is allowed to cross the slag skin flowing through the mold. As stated by Kharicha *et al.*,[8] opening the path to the mold causes reduction in the overall resistance of the ESR system. Consequently, a significant reduction of voltage is observed for Case II as demonstrated by isolines of voltage in Figure 4 (Case II). Similar to Case I, the current density becomes larger in the bulk of slag with increasing the submerged volume of electrode. In addition, the molten slag becomes colder due to high thermal conductivity of melt and low magnitude of power generated in the process. In Case II, the electrode tip develops a parabolic shape from the extremities leaving a flat tip at the center. This unique shape of electrode has been

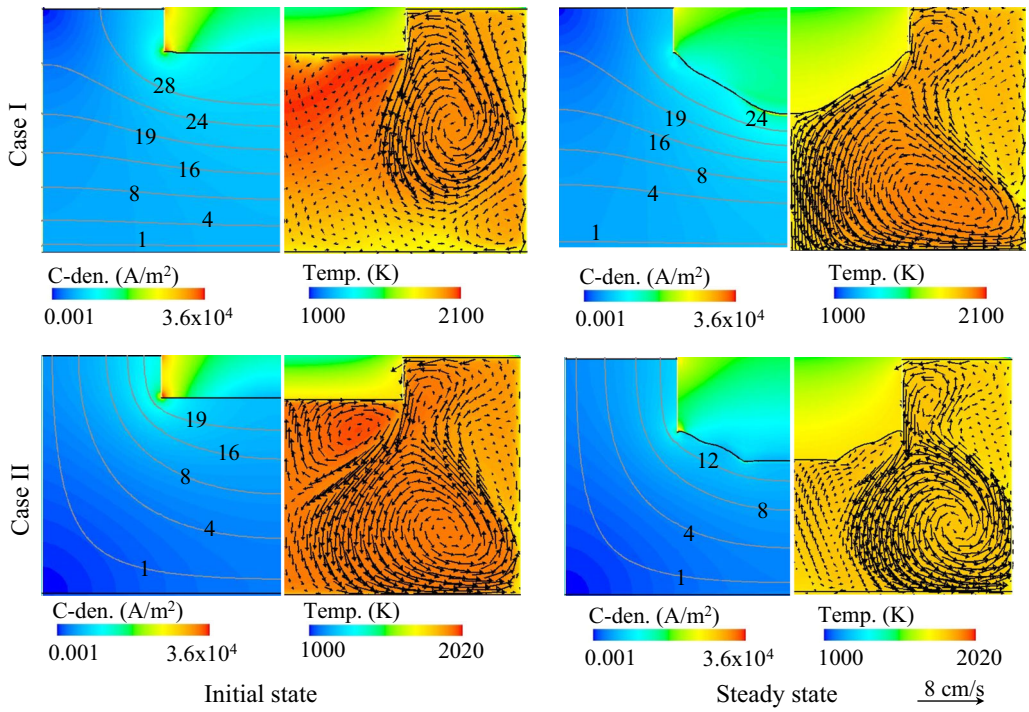

Fig. 4—Contour of current density overlaid with isolines of voltage (left half), contour of temperature overlaid with vectors of velocity (right half) for Case I (upper row) and Case II (bottom row).

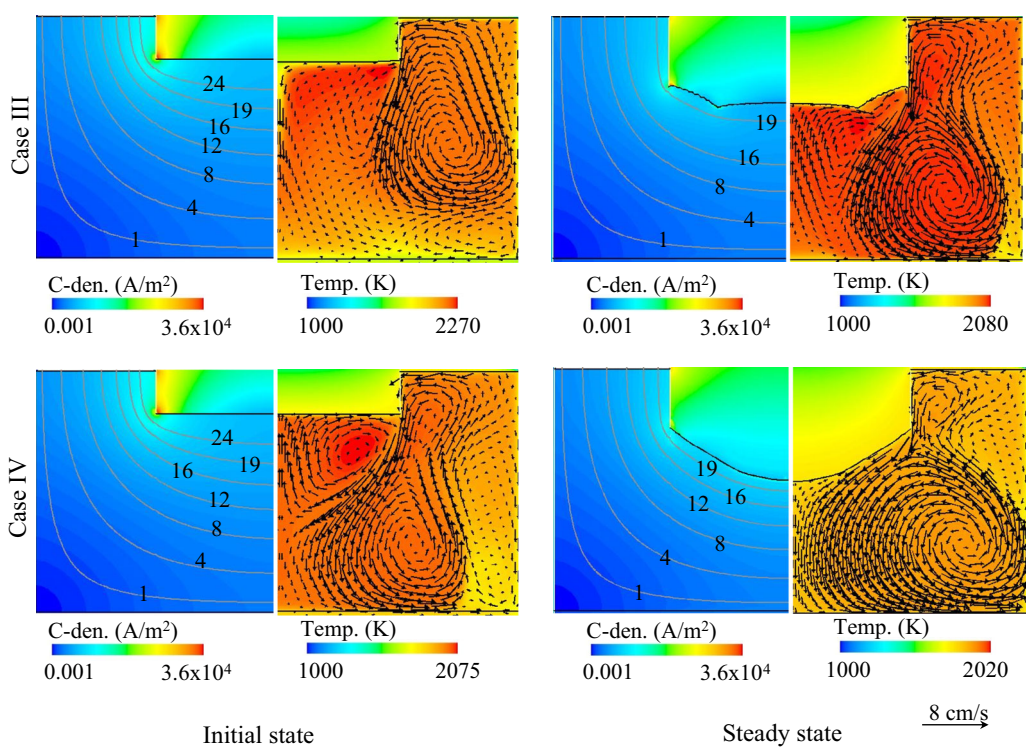

Fig. 5—Contour of current density overlaid with isolines of voltage (left half), contour of temperature overlaid with vectors of velocity (right half) for Case III (upper row) and Case IV (bottom row).

previously observed in both simulation[20] and real process.[13]

3. *Case III*

A lower electrical conductivity and lower thermal conductivity of the slag are assumed, and the current is allowed to cross the slag skin flowing through the mold. The lower electric conductivity of slag results in higher generated power in the system. Significant amount of Joule heating is released under the shadow of electrode where the current density is fairly large .With the increase of immersion depth, the reduction in total voltage is observed as shown using isolines of voltage for initial and final steady states. Note that, the global energy transfer is weak due to low thermal conductivity of molten slag. As a consequence, the bulk of molten slag becomes very hot as shown in Figure 5 (Case III). The immersion depth is shallow, and the electrode tip develops a relatively flat concave shape.

4. *Case IV*

The molten slag in Case IV is considered thermally a better conductor compared to the former case. Consequently, the heat transfer is efficient in the slag zone resulting in colder slag compared to Case III as indicated in Figure 5 (Case IV). The current density is intensified in the bulk of slag with the increase of electrode immersion depth. Thus, the Lorentz force becomes dominant resulting in promotion of stirring in slag zone. The electrode is deeply immersed into the slag zone at the steady state. Therefore, a significant reduction of the voltage is observed comparing the initial and final steady states for Case IV. In addition, the amount of released Joule heating is notably decreased during the process for this case. Finally, electrode tip develops a parabolic shape.

IV. DISCUSSION

The melting rate and shape of electrode tip are important indicators of the ESR process, and they determine the efficiency of system. The predicted shape of electrode tip is compared with the experimentally observed one (Figure 6). A fairly good agreement with the experiment is obtained for Case I and Case IV. Additionally, the power generation predicted by Case I and Case IV agrees with the experiment as well (Table V). The heat can efficiently transfer to the electrode due to large thermal conductivity of the slag (~5 W m^{-1} K^{-1}). In fact, the turbulent flow in the bulk of slag zone can dramatically increase the effective thermal conductivity of the slag (~84 to 973 W m^{-1} K^{-1}) as described by Choudhary and Szekely.[47] As illustrated in Figure 7, the effective thermal conductivity is significantly increased by the turbulence, and it leads to a strong enhancement of heat transfer in the bulk slag. Thus, the temperature remains relatively uniform in the bulk as shown in Figures 4 and 5. On the other hand, the effective turbulence thermal conductivity gradually decreases from the bulk to the region near walls where it has the same order of magnitude as molecular thermal conductivity due to damping of turbulence near walls.[27–29] The main difference between Case III and Case IV is the molecular thermal conductivity of slag. The heat transfers to the boundaries such as mold, air, or electrode are minimized for Case III leading to high temperature in the slag zone. As a consequence, the melt rate becomes large and the immersion depth decreases. In other words, increasing thermal conductivity of slag will lead to a decrease of melt rate. It must be noted that significant differences are observed regarding to the shape of electrode tip and the immersion depth between Case III and Case IV despite similar power generation. Thus, the voltage drop and subsequently power generation depend on both immersion depth and shape of electrode tip. A comparison is made between Case I and Case II to explore the effect of current path (without and with mold current). The amount of power generation and temperature is larger and higher for Case I (without mold current) that causes higher melt rate as described in Table V. The shape of tip for Case II is quite similar to Case III although the thermal and electrical conductivities are noticeably different. The immersion depth is approximately the same

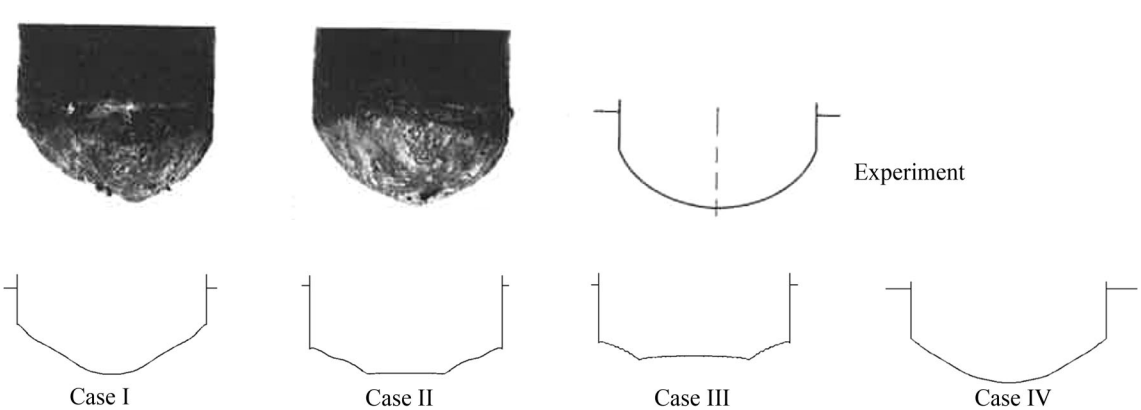

Fig. 6—Shape of electrode tip observed in experiment conducted (upper row) by Tacke and Schwerdtfeger,[17] numerically simulated shapes of electrode tip of 4 Cases (bottom row).

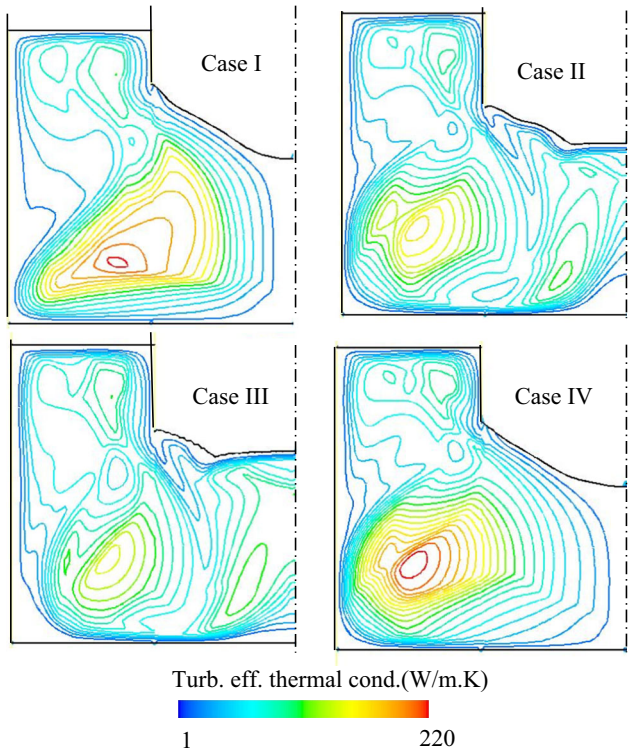

Fig. 7—Isolines of effective thermal conductivity due to turbulence for simulation cases.

for all cases except Case III which has the highest melting rate and lowest immersion depth. For the latter, the highest temperature in slag zone is observed among all cases due to low molecular thermal conductivity and inefficient heat transfer through the walls.

In a real ESR process, the stability is achieved by including a control system on electrode immersion depth to avoid undesirable extreme cases happening (the electrode tip touches melt pool). Therefore, it is necessary to apply a numerical adaptation of electrode immersion depth as described in Eq. [17]. It should also be stated that the choice of $l_{\min}$ and $l_{\max}$ in Eq. [17] might influence the feeding velocity of electrode (u_E) and consequently the melt rate and shape of electrode tip of steady state. For that, further investigations are demanded. According to Table V, approximately equivalent ratios (power generation to melt rate) are obtained for Case I and Case IV at steady state in which the shape of electrode tip is fairly similar. Additionally, Case II and Case III are following the same behavior due to insignificant difference in the ratio calculated at steady state. In conclusion, the shape of electrode tip at steady state is much similar for ESR processes running with the same ratio of power generation to melt rate.

The predicted melt rate for all cases is always lower than the value reported from the experiment (Table V). This indicates that the amount of heat provided to electrode is underestimated by simulations. The current model does not take into account electrochemical polarization overpotential, enhancement of turbulence in the slag bulk due to droplet dripping, and formation of liquid film under the electrode. Departure of droplets from the electrode can generate stronger turbulence in the slag bulk that certainly enhances the global energy transfer and melt rate.[23,24] In order to improve the quantitative accuracy of the numerical result, the aforementioned factors must be included in the future model.

V. SUMMARY

A 2D axisymmetric numerical model was applied to simulate the electrode melting during ESR process. The submerging and remelting of electrode is modeled using a dynamic mesh-based approach. The shape of electrode tip at the steady state validated against an experiment. The following conclusions were made:

1. The dynamic mesh-based approach is proved to be a successful method to model the electrode shape. The simulation results agree with the experimental fact that with the increase of melt rate, the immersion depth decreases when the magnitude of imposed current is kept constant. Furthermore, the ratio of power generation to melt rate, called power consumption, is an important factor to determine the shape of electrode: it is observed that the shape of electrode remains almost the same when the ratio is kept constant.
2. The voltage drop and subsequent power generation in the system are governed by both immersion depth and shape of electrode tip. In other words, similar power generation is observed for systems where the shapes of tip and immersion depth were different. Therefore, the melt rate, immersion depth, and shape of electrode tip are interdependent parameters.

The total power generation and the efficiency of global heat transfer in the system are highly dependent on the molten slag physicochemical properties such as electrical and thermal conductivities. Due to difficulty of measurements of properties, a large uncertainty of the properties exists. Therefore, parameter studies by varying the electrical and thermal conductivities of slag are made. It is found that

3. The electrical conductivity of slag (liquid and solid) mainly influences the electric current path which impacts the velocity and temperature distribution in the process. As a consequence of different electric current paths, the power generation, melt rate, and shape of electrode are significantly influenced.
4. The thermal conductivity of slag determines the efficiency of global heat transfer in the process. Increasing thermal conductivity of slag will result in decreasing melt rate.

To improve the quantitative accuracy of the modeling results, the following phenomena must be included to the current model. Firstly, it is essential to incorporate the effect of droplets dripping through the slag into the model. Secondly, it is necessary to include the influence of electrochemical polarization overpotential since the electric current is conducted by ions in the slag.

ACKNOWLEDGMENTS

The authors acknowledge the financial support by the Austrian Federal Ministry of Economy, Family and Youth and the National Foundation for Research, Technology and Development within the framework of the Christian Doppler Laboratory for Advanced Process Simulation of Solidification and Melting.

REFERENCES

1. G. Hoyle: *Electroslag Processes*, Applied Science Publishers, London, 1983.
2. E.J. Pickering: *ISIJ Int*., 2013, vol. 53, pp. 935–49.
3. G. Hoyle: *6th International Vacuum* Metallurgy *Conference on Special Melting*, San Diego, 1979, pp. 624–40.
4. W. Holzgruber: *5th International Symposium on Electroslag and Other Special Melting Technologies*, Pittsburgh, 1974, pp. 70–91.
5. A. Mitchell: *Perspective in Metallurgical Development Conference*, Sheffield, England, 1984, pp. 89–98.
6. F.S. Suarez, J.E. Roberts, and L.D Schley: *5th International Symposium on Electroslag and Other Special Melting Technologies*, Pittsburgh, 1974, pp. 126–45.
7. A. Mitchell: *Electric Furnace Steelmaking Conference*, ISS, Warrendale, PA, 1985, p. 212.
8. A. Kharicha, E. Karimi-Sibaki, M. Wu, and A. Ludwig: *International Symposium on Liquid Metal Processing and Casting*, Austin, 2013, pp. 95–99.
9. D.K. Melgaard, J.J. Beaman, and G.J. Shelmidine: U.S. Patent 7,180,931 B1, 2007.
10. D.K. Melgaard, G.J. Shelmidine, and B.K. Damkroger: U.S. Patent 6,496,530 B2, 2002.
11. D.K. Melgaard, R.L. Williamson, and J.J. Beaman: *JOM*, 1998, vol. 50, pp. 13–17.
12. A. Kharicha, M. Wu, and A. Ludwig: *International Symposium on Liquid Metal Processing and Casting*, Austin, 2013, pp. 145–50.
13. M. A. Maulvault: Ph.D. Thesis, MIT, 1967, pp. 80–85.
14. A. Mitchell, S. Joshi, and J. Cameron: *Metall. Trans*., 1971, vol. 2, pp. 561–67.
15. J. Mendrykowski, J.J. Poveromo, J. Szekely, and A. Mitchell: *Metall. Trans*., 1972, vol. 4, pp. 1761–68.
16. T. Kishida, K. Yamaguchi, T. Tomioka, and T. Ichihara: *Electr. Steel*, 1974, vol. 45, pp. 219–27.
17. K.H. Tacke and K. Schwerdtfeger: *Arch. Eisenhüttenwesen*, 1981, vol. 52, pp. 137–42.
18. A. Jardy, D. Ablitzer, and J.F. Wadier: *Metall. Trans. B*, 1991, vol. 22, pp. 111–20.
19. J. Yanke, K. Fezi, M. Fahrmann, and M.J.M. Krane: *International Symposium on Liquid Metal Processing and Casting*, Austin, 2013, pp. 47–55.
20. A. Kharicha, M. Wu, and A. Ludwig: *ISIJ*, 2014, vol. 54, pp. 1621–28.
21. A. Mitchell and G. Beynon: *Metall. Trans*., 1971, vol. 2, pp. 3333–45.
22. M. Kawakami, K. Nagata, M. Yamamura, N. Sakata, Y. Miyashita, and K.S. Goto: *Testsu- to-Hagane*, 1977, vol. 63, p. 220.
23. A. Kharicha, A. Ludwig, and M. Wu: *EPD Congress*, San Diego, USA, 2011, pp. 771–78.
24. A. Kharicha, M. Wu, A. Ludwig, M. Ramprecht, and H. Holzgruber: *CFD modeling and simulation in materials*, Wiley, Florida, 2012, pp. 139–46.
25. V. Weber, A. Jardy, B. Dussoubs, D. Ablitzer, S. Ryberon, V. Schmitt, S. Hans, and H. Poisson: *Metall. Mater. Trans. B*, 2009, vol. 40B, pp. 271–80.
26. H. Song and N. Ida: *IEEE Trans. Magn*., 1991, vol. 27, pp. 4012–15.
27. T. Esch and F. R. Menter: *Turbulence Heat and Mass Transfer Conference*, Antalya, Turkey, 2003.
28. F.R. Menter: *AIAA J*., 1994, vol. 32, pp. 1598–605.
29. F.R. Menter, M. Kuntz, and R. Langtry: *Turbul. Heat Mass Transf*., 2003, vol. 4, pp. 625–32.
30. Fluent 14.5 User's Guide, Fluent Inc., 2012.
31. A. Menendez Blanco and J.M. Fernandez Oro: *Comput. Fluids*, 2012, vol. 57, pp. 138–50.
32. G. Lame and B.P. Clapeyron: *Ann. Chem. Phys*., 1831, vol. 47, pp. 250–56.
33. L.I. Rubinstein: *The Stefan Problem*, American Mathematical Society, Providence, 1971.
34. K.C. Mills and B.J. Keene: *Int. Met. Rev*., 1981, vol. 1, pp. 21–69.
35. M. Hajduk and T.E. Gammal: *Stahl Eisen*, 1979, vol. 99, p. 113.
36. K.M. Kelkar, S.V. Patankar, S.K. Srivatsa, R.S. Minisandram, D.G. Evans, J.J. deBarbadillo, R.H. Smith, R.C. Helmink, A. Mitchell, and H.A. Sizek: *International Symposium on Liquid Metal Processing and Casting*, Austin, 2013, pp. 3–12.
37. A.D. Patel: *International Symposium on Liquid Metal Processing and Casting*, Nancy, France, 2011, pp. 49–56.
38. S.F. Medina and M.P. de Andres: *Ironmak. Steelmak*., 1987, vol. 14, pp. 110–21.
39. E. Karimi-Sibaki, A. Kharicha, M. Wu, and A. Ludwig: *International Symposium on Liquid Metal Processing and Casting*, Austin, 2013, pp. 13–19.
40. E. Karimi-Sibaki, A. Kharicha, M. Wu, and A. Ludwig: *Ingot Casting Rolling Forging Conference*, Milan, Italy, 2014.
41. H. Holzgruber, W. Holzgruber, A. Scheriau, M. Knabl, M. Kubin, J. Korp, and R Pierer: *International Symposium on Liquid Metal Processing and Casting*, Nancy, France, 2011, pp. 57–64.
42. M. Hugo, B. Dussoubs, A. Jardy, J. Escaffre, and H. Poisson: *International Symposium on Liquid Metal Processing and Casting*, Austin, 2013, pp. 79–85.
43. A. Kharicha, A. Ludwig, and M. Wu: *Mater. Sci. Eng. A*, 2005, vols. 413–414, pp. 129–34.
44. E. Karimi-Sibaki, A. Kharicha, J. Korp, M. Wu, and A. Ludwig: *Met. Trans. Forum*, 2014, vol. 790, pp. 396–401.
45. A. Kharicha, W. Schützenhöfer, A. Ludwig, R. Tanzer, and M. Wu: *Steel Res. Int*., 2008, vol. 79, pp. 632–36.
46. R. Taylor and K.C. Mills: *Arch. Eisenhüttenwesen*, 1982, vol. 53, pp. 55–63.
47. M. Choudhary and J. Szekely: *Ironmak. Steelmak*., 1981, vol. 5, pp. 225–32.